Visualizing the distribution of water in nominally anhydrous minerals at the atomic scale: Insights from atom probe tomography on fayalite

Jia Liu[1*+], Sandra D. Taylor[2*+], Odeta Qafoku[3], Bruce W. Arey[1], Robert Colby[3,§], Arielle Eaton[3], Jonah Bartrand[3], Vaithiyalingam Shutthanandan[3], Sandeep Manandhar[3], and Daniel E. Perea[3*]

[1] Energy and Environment Directorate, Pacific Northwest National Laboratory, Richland, WA 99354, USA

[2] Physical & Computational Sciences Directorate, Pacific Northwest National Laboratory, Richland, WA 99354, USA

[3] Earth & Biological Sciences Directorate, Pacific Northwest National Laboratory, Richland, WA 99354, USA

[+]Co-first authors

[§] Present address: Corporate Strategic Research, ExxonMobil Research and Engineering Company, Annandale, New Jersey 08801, USA.

*Corresponding Authors: J. L. (jia.liu@pnnl.gov), S. D. T. (sandra.taylor@pnnl.gov), D. E. P. (daniel.perea@pnnl.gov)

Prepared for submittal to Geophysical Research Letters

Key points

- At the planetary scale nominally anhydrous minerals are significant water reservoirs, but the mode of incorporation is poorly understood.
- Hydrated interlayers and minor element partitioning in fayalite are visualized at the near atomic level using atom probe tomography.
- This approach provides unique insight into the distribution of water in geomaterials, enabling a deeper understanding of their properties.

Abstract

Nominally anhydrous minerals (NAM) such as olivine are important reservoirs for water in the Earth's upper mantle, although the association of water with crystallographic defects is poorly understood. Here, hydrated regions at the atomic scale in fayalite (Fe_2SiO_4) are directly resolved using atom probe tomography. Site-specific analyses reveal regions that are either compositionally homogenous or contain nanometer-long channels that are consistent with hydrated defects. Na as a minor element is also enriched within the interlayers, indicating the formation environment is associated with Na geochemically. The ability to directly visualize and characterize hydrated regions at the nanometer scale can provide critical insight into the material properties of NAM and their impact on planetary-scale processes, such as the influence of water-bearing minerals on mantle rheology and geodynamics.

Plain language summary

Anhydrous minerals such as olivine, containing seemingly small amounts of water per unit volume, are significant reservoirs of water on Earth and play a critical role in planetary geodynamics. Our knowledge of how water incorporates into these minerals is however lacking because it is challenging to actually see where the water resides in the crystal structure at the atomic scale. Here, we utilize the novel chemical imaging technique atom probe tomography to map water within minerals in three dimensions atom-by-atom. We find signatures for water within nanometer-long structurally defective channels in the crystal. Sodium, thought to be a constituent of the formation environment, is also found to coincide with these defects. While the mode of water incorporation in minerals has been speculated for decades, our observations are important

because it provides the first direct evidence for this occurrence. The approach developed here can be further applied to understand mechanisms for water incorporation in minerals in various environments. By understanding the fundamental properties of minerals at the atomic level, we can gain important insight into processes at the planetary scale such as the influence of water-bearing minerals on mantle rheology.

Keywords

atom probe tomography, water, defects, nominally anhydrous mineral, olivine

1. Introduction

While the chemical formulas of mantle-derived minerals such as olivine ($(Mg,Fe)_2SiO_4$) indicate they are anhydrous, they are capable of structurally incorporating small amounts of hydrogen (H) as hydroxyl (OH) (colloquially referred to as water) (Demouchy & Bolfan-Casanova, 2016). At the planetary scale, these nominally anhydrous minerals (NAM) may, in turn, be significant repositories of mantle water. Thus, understanding the occurrence of water in NAM and its incorporation mechanisms has broad implications, from understanding planetary evolution to the determination of Earth's water budget. For instance, the presence of water in NAM influences mantle rheology, lubricating and facilitating the movement of faults via hydrolytic weakening (Sommer et al., 2008), as well as its electrical conductivity (Karato, 1990). Additionally, the insight gained from NAMs on Earth can be utilized to understand the evolution of planetary systems like that of Mars (Peslier, 2010).

Quantification of water in NAM has been extensively studied for the last three decades (Bell et al., 2003), though understanding its mode of incorporation is largely ambiguous due to challenges in directly observing the distribution of water at the atomic level. That is, the amount of H in NAM is readily obtained using infrared (IR) spectroscopic, elastic recoil detection analysis (ERDA) (Bolfan-Casanova et al., 2018; Withers et al., 2012), and secondary ion mass spectrometry (SIMS) techniques (Bell et al., 2003; Koga et al., 2003; Kurosawa et al., 1992), implying its existence in structural point defects. It is speculated that H can also be heterogeneously distributed and localized within higher-dimensional defects, such as in planar defects, comprised of either a separate hydrous phase or an ordered array of point defects, or inclusions of hydrous minerals or aqueous water (Demouchy, 2010a, 2010b; Drury, 1991; Mosenfelder et al., 2006). Large cations and compounds may sit within dislocations or other defects rather than substituting into the mineral lattice (Beran & Libowitzky, 2006). Indirect evidence has been gained through microstructural characterization of defects, largely grain boundaries, in NAM by high-resolution transmission electron microscopy (HRTEM) complemented by IR-measurements (Hiraga et al., 2004; Khisina & Wirth, 2002), as well as synchrotron-based Fourier-Transform Infrared (FT-IR) measurements (Sommer et al., 2008). 2D-FTIR is another method which can reveal the micrometer-sized impurities in the natural samples

(Potrafke et al., 2020). However, due to technical limitations with sensitivity and spatial resolution, direct visualization and measurement of water associated with crystallographic defects at the nanometer scale has not been achieved, precluding understanding of its influence on NAM properties.

Atom probe tomography (APT) is a powerful analytical technique enabling direct visualization of the elemental and isotopic distributions in three dimensions (3-D), with sub-nanometer spatial resolution and part-per-million elemental sensitivity (M. K. Miller, 2000). It has gained significant interest within geosciences in recent years, where novel observations of nanoscale chemical heterogeneities across a broad range of geologic materials have led to a deeper understanding of various geochemical and physical phenomena (Reddy et al., 2020, refs therein). Furthermore, APT has been alluded to as a means to detect and map water within geological materials (Daly et al., 2020), due to its ability to potentially resolve hydride signatures in materials. However, APT based studies demonstrating this ability are limited; for instance, nanoscale fluid inclusions have been inferred in pyrite (FeS_2) based on the presence of nanometer-scale O-rich clusters in the matrix (Dubosq et al., 2020), although distinct chemical signatures pertinent to water were difficult to resolve. Here, we utilize APT to map the distribution of water in a natural fayalite specimen (Fe_2SiO_4) at the atomic scale. Hydride species are readily detected and utilized to reveal hydrated interlayers along with partitioning of minor elements within the fayalite, providing unprecedented insight into water incorporation in NAM. Ultimately this approach can be used to study incorporation mechanisms with implications across a broad range of fields from understanding planetary water reservoirs to mantle rheology.

2. Sample preparation and analysis conditions

The natural fayalite specimen was obtained from Crystal Park, El Paso, Colorado through Ward's Natural Science (49-5925). The sample was analyzed in detail by X-ray diffraction, Mössbauer spectroscopy, and electron microprobe analysis (Qafoku et al., 2012), confirming the phase is fayalite with minor impurities (i.e., 3.2 % Mn-based from microprobe analysis). The sample was polished following the standard metallographic polishing procedure with final polishing with 1 µm diamond. The sample microstructure and microscopic chemistry were imaged in local areas using scanning electron microscopy (SEM) and energy dispersive spectroscopy (EDS) analyses, respectively. These analyses in turn informed regions to analyze by APT.

Scanning transmission electron microscopy (STEM) and electron energy loss spectroscopy (EELS) was also performed. TEM data were acquired with a probe-corrected FEI Titan operated at 80 kV, equipped with a Gatan Quantum spectrometer. Data were processed with Gatan Microscopy Suite and Hyperspy (Peña et al., 2021).

Given the recent but rapidly growing adoption of APT in the geosciences, we briefly describe the general protocol and principles for APT analysis. The reader is referred to Miller and Forbes (2014) book for further information on the principles and Reddy et al. (2020) for examples of its applications within the geosciences. Needle-shaped specimens for APT analysis were prepared using a dual-beam focused ion beam/scanning electron microscope (FIB/SEM; FEI Helios 600 Nanolab), following conventional lift-out techniques . In brief, a protective Pt capping layer was deposited on a rectangular section of the specimen surface (e.g., ~3 × ~20 µm) in the region(s) of interest by electron- and ion-beam induced deposition within the dual-beam SEM, protecting the sample from implantation damage and Ga contamination during Ga ion milling. A lamellar wedge (~20 µm long) was created by trench milling on both sides of the region with the ion beam (Ga^+ ion, 30 kV). The region was extracted with the Omniprobe micromanipulator, and sections were mounted over several Si microposts. Each section was annularly milled to obtain needle-shaped specimens with <100 nm tip diameter.

APT analysis (B. Gault et al., 2012; Miller & Forbes, 2014) was conducted using a CAMECA LEAP 4000X HR equipped with an ultraviolet (λ=355 nm) wavelength laser and a reflectron lens enabling an enhanced mass resolution. During APT analysis, the needle-shaped specimen is cryogenically-cooled and placed under a strong electric field within an ultra-high vacuum chamber. Field evaporation of individual atoms as positively charged ions from the tip apex is induced by a pulsed UV laser pulsed. The evaporated species are accelerated towards a position-sensitive detector which records the relative position of each detected ion. Simultaneously, the mass of each detected ion is determined from time-of-flight mass spectrometry. From this information, the specimen's original atomic arrangement is reconstructed in 3D. These specimens were held at a temperature of 44 K in an ultrahigh vacuum (~1.6 x 10^{-9} Pa). Picosecond laser pulses with energies between 10-40 pJ were applied to the specimen tip with the pulse frequency of 100 kHz. The detection rate remained at 0.3%, corresponding to 3 detected ion evaporation events for every 1000 pulses.

3D composition point cloud maps were reconstructed using the position and time-of-flight of each individual detected ion by employing the integrated visualization and analysis software (IVAS 3.6.6) developed by CAMECA (Madison, WI). To produce the quantitatively-scaled reconstruction, the correlative electron microscopy image was used, as further described in the Supplementary Information (SI; Figure S1). To reconstruct the specimen chemistry, mass peaks within the generated spectra were assigned identities based on the relative mass, measured elemental compositions and expected isotopic compositions based on natural abundance (NA). Elemental compositions were calculated relative to the total counts detected within the measured volume and isotopic compositions were measured as ratios relative to the most dominant isotope peak. Furthermore, given the multi-elemental and isotopic nature of this specimen, potential peak overlaps from isobaric and/or polyatomic interferences were also considered. That is, contributions from multiple ionic species within a given mass peak could be deconvoluted by comparing the measured integrated mass peak intensity to expected isotopic compositions (based on NA), where measurable deviations indicate the presence of additional chemical components, as highlighted in the results (Johnson, Thuvander, Stiller, Odén, et al., 2013). The analyses were performed consistently across the specimens.

3. Results

SEM imaging shows the general microstructure of the fayalite (Figure 1). Two distinct regions are revealed using backscattered electron imaging: (1) long thin regions with relatively homogeneous and higher backscatter electron intensity, and (2) regions with banded patterns of light and dark features. These regions are respectively referred to as regions 1 and 2. The darker regions appear fractured, suggesting differences in rheology between the two areas. Both regions are consistent with fayalite based off on compositional analyses with EDS (26 atomic % Fe (at.%), 15 at.% Si and 58 at.% O); the dark region and bright region differ by ~2 at.% Fe which is within error of EDS analysis. Three needle-shaped tips were prepared from each region via FIB-SEM and were successfully measured by APT, using the conditions described earlier. In the main text we describe the results of one tip from each region in detail as representative samples. Atom maps of the two tips from region 2 are presented in the SI (Figure S2).

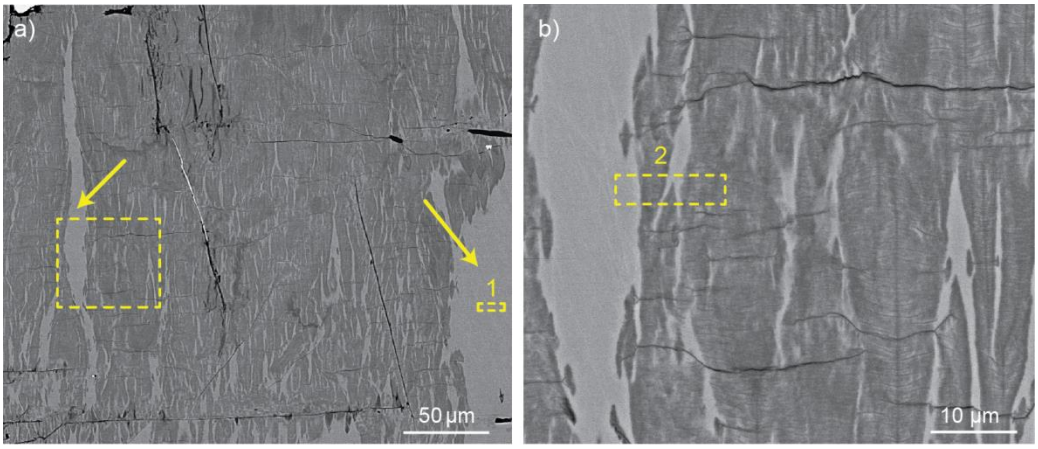

Figure 1 Backscattered electron image of the polished fayalite specimen. (a) Representative microstructure showing the light contrast regions (Region 1) flanked by darker contrast regions (Region 2). (b) Higher-magnification image from the area inside the rectangular box in (a), further highlighting the microstructural homogeneity in Region 1 vs. the heterogeneity and fractured nature in Region 2. Specimens from each region were prepared in the locations labeled as "1" and "2", respectively. Features (~20 µm or larger) that run perpendicular to the banded structure are discontinuous cracks.

APT analyses for region 1 are first discussed. As mentioned, the 3D chemical reconstruction of the sample required careful analysis of the mass spectrum. That is, the detected ions are collectively presented as a histogram of mass peaks (measured in Daltons, Da) within a mass spectrum, as highlighted in Figures 2a and 2b. The ions can be elemental (e.g., Fe^{+}) or small molecular species (e.g., $FeOH^{+}$) as well as singly or multiply charged (e.g., Fe^{+} vs. Fe^{2+}), and are assigned to best match the expected composition. Furthermore, due to the high mass resolving power of APT ($m/\Delta m > 1000$), individual isotopes for each species are also observed as distinct mass peaks within a subset of ionic species. In general, mass spectral analyses for specimens in region 1 confirm its elemental composition is qualitatively consistent with fayalite (Figure 2a). That is, Fe, Si, and O are major species detected in the mass spectrum, as expected, along with metal- and silicon-oxide ions (e.g. FeO^{2+} and SiO^{+} species at 35 – 37 Da and 44 – 46 Da, respectively) (Figure 2b). Their isotopes were also readily resolved in the mass spectra and their compositions were largely consistent with the NA based on peak deconvolution; e.g., the peaks at 44, 45, and 46 Da assigned to SiO^{+} solely belong to its isotopes $^{28}Si^{16}O^{+}$, $^{29}Si^{16}O^{+}$, and $^{30}Si^{16}O^{+}$, respectively.

In addition to the major elements, minor elements such as Ca, Mg, Mn, and Li were also detected, which are common impurities in naturally occurring fayalite and other olivines (Krivolutskaya & Bryanchaninova, 2011). EDS and proton-induced X-ray emission (PIXE) analyses are unable to resolve the light elements like Li but largely corroborate the APT results (see SI Figure S3). Furthermore, the distribution of the major and minor elements (i.e., Fe, Si, O, Mg, Ca, and Mn) is found to be homogeneous throughout the sample volume, suggesting the area sampled in region 1 represents the bulk phase (Figure 2c).

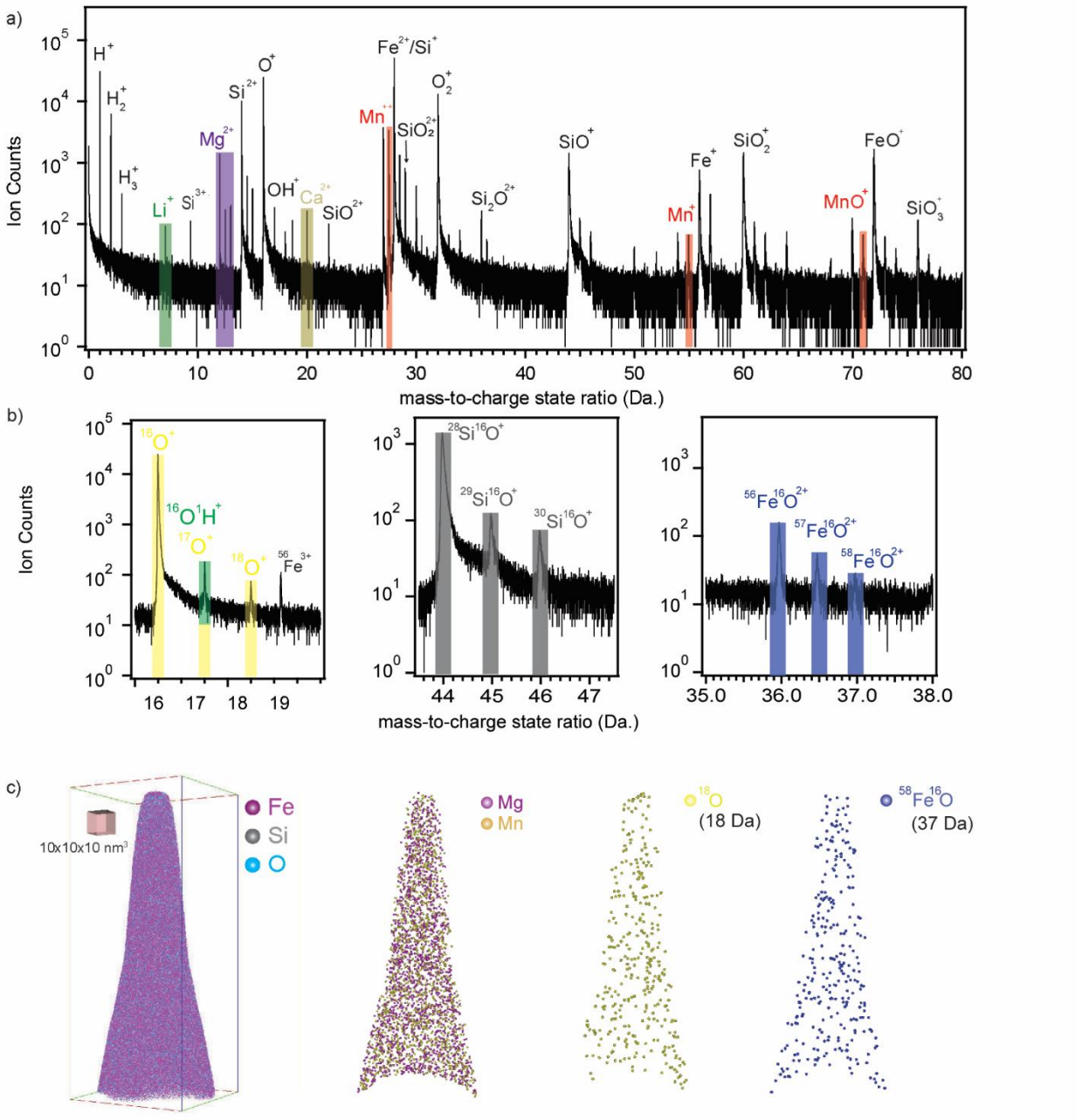

Figure 2 Mass spectra (a-b) and 3D chemical reconstruction of fayalite from region 1 (c). (a) APT mass spectra showing the ion

assignment used for compositional measurements in region 1. (b) Mass spectra specifically highlighting isotopic analyses of significant oxide peaks including O^+, SiO^+, and FeO^{2+}. The relative contributions from various ions are denoted by the intensity of the colored bars; e.g. based off of the expected elemental and NA compositions, the peak at 16 Da is attributed to $^{16}O^+$ while that at 17Da is attributed to $^{16}O^1H^+$ (green bar), with negligible contributions from $^{17}O^+$ (yellow bar). (c) Atomic maps of the major (i.e., ^{54}Fe, Si, and O) and minor elemental (Mg, Mn) species observed in region 1. For clarity, only 5% of Fe, Si, and O atoms are shown. The distribution of Mg (^{24}Mg, ^{25}Mg, ^{26}Mg), Mn, ^{18}O, and $^{58}Fe^{16}O$ were taken from a sliced region with 5 nm thickness. The unit cube represents a volume of 10×10×10 nm^3.

While the elemental detection sensitivity with APT is reliable based on comparison to other analytical mapping techniques, quantification of the fayalite stoichiometry is complicated. The measured O concentration in the bulk regions (~43 at.%) deviates from expected, which is a known issue for APT analysis of oxides in general (Devaraj et al., 2013; Baptiste Gault et al., 2016). Additionally, the average composition of Fe and Si deviates from that expected (46 at.% and 8 at.%, respectively). This may arise from complications in the ion assignment due to isobaric interferences; e.g., the mass-to-charge state peak at 28 Da may correlate to either or both $^{56}Fe^{2+}$ and $^{28}Si^{1+}$ species (Fig. 2a). While quantification of the Fe and Si concentrations is semi-quantitative, it is still possible to resolve the relative elemental spatial distribution within the grain by utilizing isotope masses unique to that element (Johnson, Thuvander, Stiller, Oden, et al., 2013); e.g., for Fe analyses, we consider the ^{54}Fe isotope which does not overlap with Si isotopes or isotopes from other elements detected in the specimen (Figure 2b). This approach enables a qualitative but reliable display for the 3D compositional variations within fayalite.

In comparison, APT analyses of region 2 shows it is also largely consistent with the fayalite (Figure 3a), with similar major elemental compositions to regions 1 (i.e. 43.7 at.% Fe, 10.4 at.% Si, and 41.9 at.% O from region 1; 40.5 at.% Fe, 9.9 at.% Si, and 43.6 at.% O from region 2). However, there is a measurable amount of hydrated species in region 2 which are heterogeneously distributed and localized within nanoscale domains. That is, oxide species are again observed in the mass spectrum for region 2, although interestingly related-hydroxide species are prevalent, existing as OH_x^{1+}, $FeOH_x^{1+/2+}$, and $SiOH_x^{1+/2+}$ (Figure 3b). The minor elements Mg, Mn, Ca, and Li are also detected, however measurable amounts of Na is observed in region 2 which are absent from region 1.

Comparison between the mass spectra and isotopic ratios between regions 1 and 2 provides confidence in our ion identification. Oxide species are readily identified in region

1 but hydroxide species are absent (Figure 2a, b), except for a small amount of $^{16}O^{1}H^{+}$ (17Da) which arises from residual gas present in the APT analysis chamber (Kaspar et al., 2021). In contrast, the observation of hydroxide species in the mass spectra for region 2 is evident (Figure 3b). Furthermore, in instances where hydroxide mass peak overlaps with an oxide mass peak, we were able to confirm the ion identity by peak deconvolution and comparison to expected NA ratios. As an example, the 18 Da peak is present in both regions but is found to represent $^{18}O^{+}$ in region 1 *vs.* $^{16}O^{1}H_{2}^{+}$ in region 2. That is, the ratio for the peak signal at 18Da in region 1 is quantified relative to the signal for $^{16}O^{+}$ at 16Da (18 Da ion counts/16 Da ion counts = 0.0039), and is within reason of that expected for oxygen isotopes at NA (i.e., $^{18}O/^{16}O = 0.0021$). This indicates the peak is consistent with $^{18}O^{+}$. In comparison, the ratio for region 2 far exceeds that in region 1 and at NA (0.044). It also far exceeds any contributions for $^{17}O^{1}H^{+}$ (as shown in Figure 3b). Thus, the peak at 18Da in region 2 belongs to the hydroxide species $^{16}O^{1}H_{2}^{+}$. This peak deconvolution was done across other significant hydrated mass peaks (e.g., $SiOH^{+}$ and $FeOH^{2+}$ in Figure 3b), and confirmed the prevalence of hydrated species in region 2. In turn these analyses indicate that the hydroxide species in region 2 are attributable to a hydrous component.

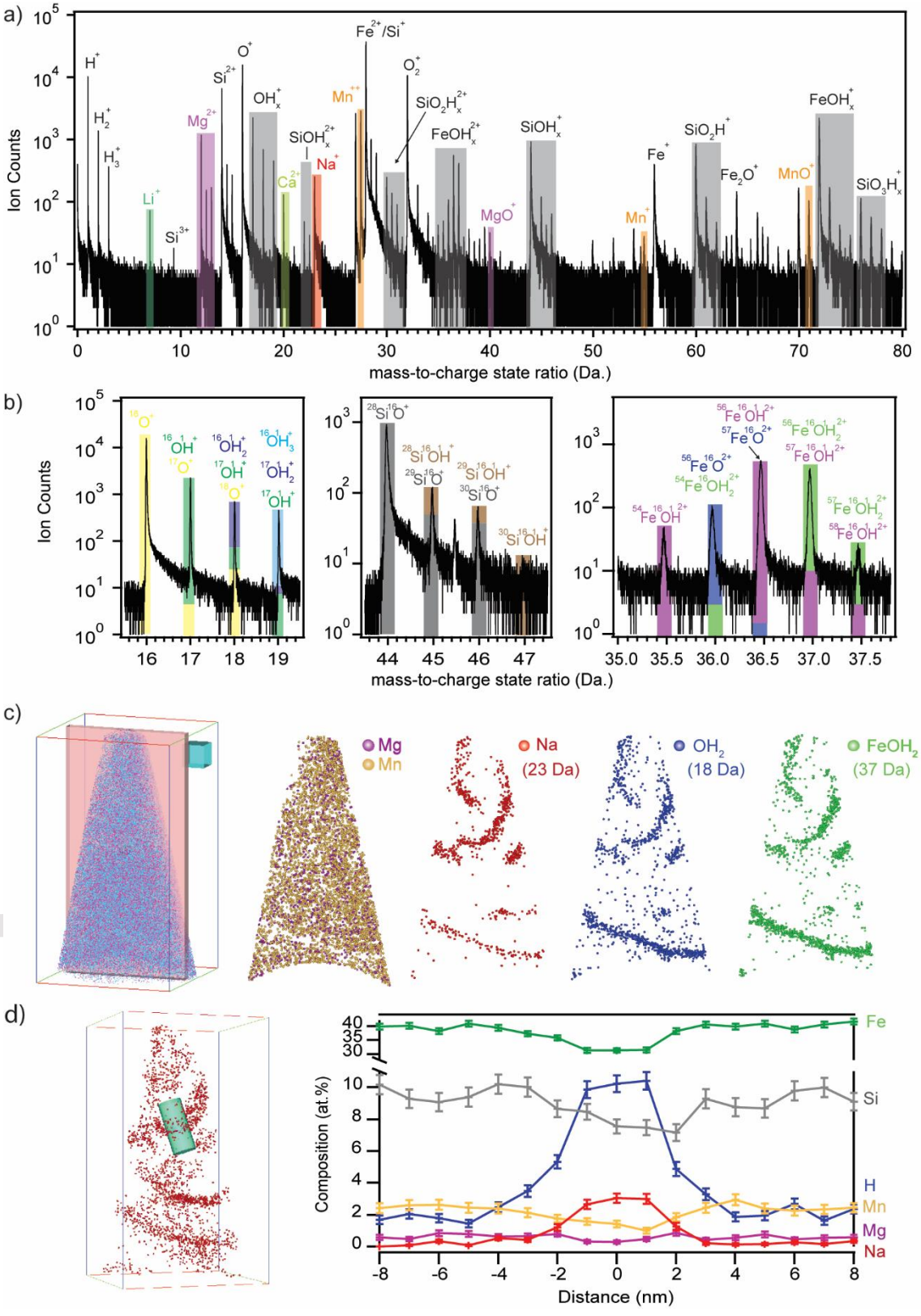

Figure 3 Mass spectra (a-b) and three-dimensional reconstruction map of natural fayalite from region 2 (c). (a) APT mass spectra showing the ion assignment used for compositional measurements in region 1. (b) Mass spectra specifically highlighting identification of the minor element Na and the isotopic analyses of significant hydroxide peaks including OH^+, $SiOH^+$, and $FeOH^{2+}$. The relative contributions from various ions are denoted by the intensity of the colored bars, like Fig. 2b. (c) Atomic maps of the major (i.e., ^{54}Fe, Si, and O) and minor elemental (Mg, Mn) species observed in region 1. For clarity, only 5% of Fe, Si, and O atoms are shown. The distribution of Mg (^{24}Mg, ^{25}Mg, ^{26}Mg), Mn, ^{18}O, and $^{56}Fe^{16}O^1H_2$ were taken from a sliced region with 5 nm thickness. The unit cube represents a volume of 10×10×10 nm^3. (d) Compositional analysis across a Na-rich channel, generated in the longitudinal direction of the cylindrical region.

While we can infer the ionic identity and clearly show the presence of water in site-specific regions, absolute quantification of the ion concentrations is complicated due to ionic interferences. For instance, while the 37Da peak is largely $^{56}Fe^{16}O^1H_2^{2+}$ it will have contributions from related species such as $^{57}Fe^{16}O^1H^{2+}$ (Figure 3b) that need to be accounted for. It is possible to roughly account for the concentration of each ion by peak deconvolution, although high compositional precision and accuracy measurements with APT is still under development. Rigorous evaluation of the mass spectra would be needed for absolute quantification of the hydroxide species, which is the focus of other studies (Meisenkothen et al., 2020). Here, the hydroxide species are used to qualitatively highlight the distribution of water in NAM and their concentration are regarded as semi-quantitative.

Visualization of the chemical components within region 2 shows the partitioning of Na and hydrated species to microstructural defects within fayalite (Figure 3c). The 3D reconstruction reveals a highly heterogeneous distribution of the hydrated ion species, which appear to be localized within thin channel-like interlayers of 2-4 nm thickness. The Na ions are spatially correlated with the hydrated species (e.g., OH_2^+ and $FeOH_2^+$) while minor elements like Mg and Mn are depleted from these hydrated regions. A 3D view of Na distribution within the entire analyzed volume is also shown in Supplementary Movie 4. The hydrated interlayers are also found to generally be densely concentrated within the analyzed region (~10-20 nm apart).

Measuring the elemental composition across one of the channels further highlights the enrichment and localization of Na and hydrated species in these interlayers and depletion of Mg and Mn (Figure 3d). That is, the plotted H concentration represents the water content across the channel, which was determined from summing up the counts of all species containing hydrogen (i.e., H, OH, $SiOH_x$ and $FeOH_x$ ions) without considering whether it has stronger bonding with SiO or FeO. While quantification of the hydrogen/water concentration is semi-quantitative at best,

as mentioned above, the relative compositions across the channel clearly show higher concentrations of Na and water within these features compared to the bulk (i.e., ~13 at.% H and ~1.7 at.% Na vs. an average 1.5% H and no detectable Na, respectively). Mg and Mn are found to be depleted in the channel-like interlayer, consistent with the observation in the 3D atom maps. The compositions on either side of the channel are similar to one another and are indicative the fayalite matrix (i.e., 36.9 at.% Fe, 12.0 at.% Si, and 44.6 at.% O). Overall, these observations provide strong evidence that the hydrated structures are associated with crystallographic defects as discussed below.

4. Discussion

Through this study we directly observe and map the distribution of minor amounts of water within crystallographic defects within fayalite using 3D APT for the first time, providing new insight into modes of water incorporation within low-content water-bearing materials. APT analysis was conducted on two chemically and microstructurally distinct regions within a natural fayalite specimen, as identified by BSE-SEM imaging. Region 1 was found to be chemically uniform by APT, mainly representing the bulk phase. This served as valuable a baseline for compositional analyses particularly with respect to region 2. Specifically, hydroxide species unique were detected, indicative of a hydrous component being uniquely associated with region 2. Furthermore, 3D chemical visualization of these species revealed their heterogeneous and highly localized distribution within channel-like interlayers.

Compositional variations unique to the microstructural features in region 2 was also captured. In particular, the spatial correlation between hydrated species and Na was strong, as it was only detected and observed in region 2 within channel-like hydrated interlayers. This observation is generally consistent with previous studies, as incompatible elements were shown to segregate to grain boundaries due to differences in its ionic radii and valence from that of the host cations (Hiraga et al., 2004), although its association with dislocations is not well-known or documented. Additionally, if the natural fayalite formed within a hydrous environment in mantle garnet, which is associated geochemically with other incompatible elements such as Na, the element will reflect an association with OH in the microstructure (Bell & Rossman, 1992). Although knowledge of this particular specimen's

environment and history are not well documented, we speculate that the strong association between water and Na and their partitioning to defects indicates that the fayalite formed or equilibrated in a hydrous environment where water is associated geochemically with an element like Na. Also, Mg and Mn were observed to be depleted from the hydrated interlayers which is the result of incompatibility of OH in the NAM (Bell & Rossman, 1992).

Although the APT results provide clear evidence of the segregation of hydrated species and minor elements to defects, what is not clear is the physical nature of the defects. To provide some insight, structural and spectroscopic chemical analysis using STEM and EELS was performed on an extracted volume from region 2 near that of which is highlighted of Fig. 1b. Annular dark field (ADF) STEM imaging readily reveals the unique microstructure within this region, as discrete linear-like defects that align relatively parallel to each other (Fig. 4a). Although such distinct microstructural defect structures are not well documented in the literature for terrestrial olivine, this microstructure bears some similarity to features attributed to dislocations previously observed in olivine from the Lafayette Martian meteorite (Lee et al., 2015).

Additional insight into the nature of the defects is provided from EELS analysis shown in Fig. 4b-4d. The ADF-STEM map (Fig. 4b) and corresponding EELS map shows the chemical partitioning of Fe(III)-like spectra to be correlated with the location of the defects, relative to the surrounding region away from the defect. To improve the signal-to-noise, the spectra shown are averages of several spectra taken from respective areas overlapping different defects and areas away from defects. The presence of Fe(III) is known to be correlated with hydrated features in olivine (Berry et al., 2005) and may be consistent with hydrous ferric oxide, corroborating the direct evidence for water incorporation within nanoscale defects in natural olivine provided by APT. We believe that the continued application APT can be conducted to resolve hydration in NAMs where specimen targeting for atomic to nanoscale structural and chemical mapping can be guided by bulk chemical/microstructural characterization including spectroscopic measurements of water content.

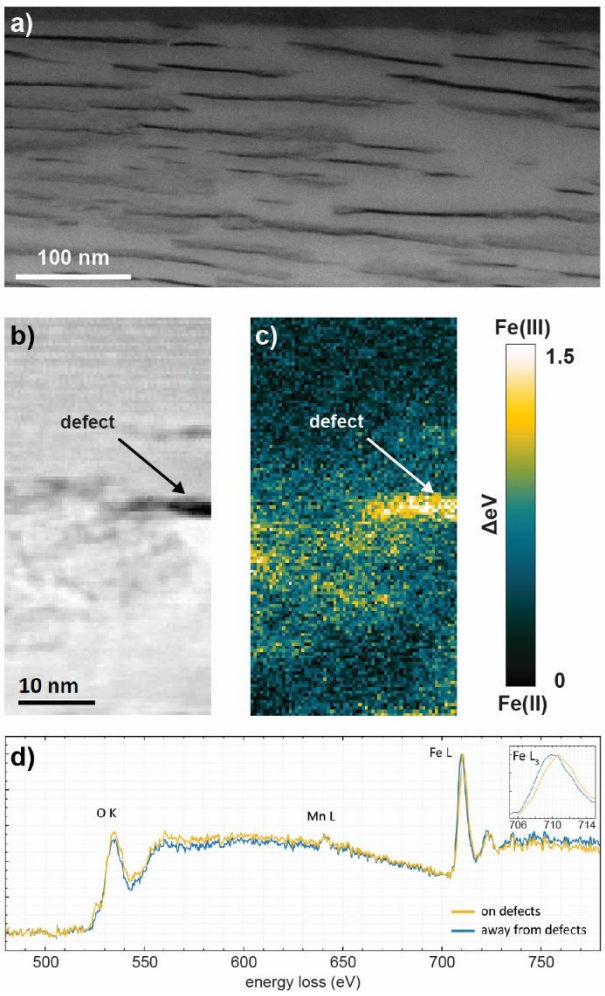

Figure 4. (a) ADF-STEM image taken in region 2 of fayalite showing the distribution of defects. (b) ADF-STEM image and correlated (c) EELS Fe L_3-edge composition map. (d) EELS spectrum spanning 480 to 780 eV taken from areas overlapping defects (e.g. mustard color star) and areas away from defects. The inset in d) is a zoomed in region of the spectra around the Fe L_3 edge which shows a shift of approximately 1 eV indicating an enhancement of Fe(III) (mustard color) spatially correlated with defects compared to the Fe(II) away from defects.

5. Conclusions

Here we demonstrate the application APT for directly mapping the distribution of water in minerals at the nanoscale, providing much-needed and long-sought-after evidence for incorporation into higher-dimensional defect structures in NAM. This paper presents new technical developments for the observation of water and trace elements in minerals at the atomic to nanoscale using atom probe tomography. While the incorporation of water in NAM into defects such as dislocations have long been predicted, it has remained speculative without direct observation and measurements at the nanometer to near atomic scale. Through the methodology developed here, water-rich defects in olivine are directly

observed and characterized, providing unprecedented insight into the unique modes for water incorporation into minerals.

This work in turn serves as a benchmark for how to probe modes of incorporation in minerals and provides new potential for connecting atomic-level phenomena to observations at the planetary scale. In combination with other multimodal analyses from IR and TEM, this approach can be applied to investigate water in NAM from various environments, providing a deeper understanding of material properties and potential impacts on far-reaching, planetary-scale processes. For instance, in regards to mantle rheology, it is important to understand water within higher-dimensional defects as these are thought to serve as efficient mechanisms for water transport through the lithosphere during solid-state deformation, thereby impacting its metasomatism and chemical buoyancy (Heggie, 1992). The ability to quantify water contents as well as directly visualize and characterize hydrated regions at the nanometer scale can thus provide critical insight into the material properties of NAM and their impact on planetary-scale processes such as the influence of water-bearing minerals on mantle rheology and geodynamics.

6. Acknowledgement

This work was supported by the Geosciences Research Program in the U.S. Department of Energy, Office of Basic Energy Sciences, Division of Chemical Sciences, Geosciences & Biosciences. A portion of the research was performed using EMSL (grid.436923.9), a DOE Office of Science User Facility sponsored by the Biological and Environmental Research program located at the Pacific Northwest National Laboratory. PNNL is operated for DOE by Battelle Memorial Institute under Contract# DE-AC06-76RLO-1830. The authors also gratefully acknowledge the contribution of Dr. Andrew R. Felmy (PNNL) as a co-author and for his valuable support of this research work. We also acknowledge Dr. Libor Kovarik (PNNL) for his useful discussions regarding the STEM-EELS analysis.

Data Availability Statement

Additional APT data, EDS and PIXE analysis and 3D movie are available in the Supporting Information and at doi.org/10.25582/data.2022-01.2412619/1838047.

References

Bell, D. R., & Rossman, G. R. (1992). The distribution of hydroxyl in garnets from the subcontinental mantle of southern Africa. *Contributions to Mineralogy and Petrology, 111*(2), 161-178. https://doi.org/10.1007/BF00348949

Bell, D. R., Rossman, G. R., Maldener, J., Endisch, D., & Rauch, F. (2003). Hydroxide in olivine: A quantitative determination of the absolute amount and calibration of the IR spectrum. *Journal of Geophysical Research-Solid Earth, 108*(B2). <Go to ISI>://WOS:000181985400002

Beran, A., & Libowitzky, E. (2006). Water in Natural Mantle Minerals II: Olivine, Garnet and Accessory Minerals. *Reviews in Mineralogy and Geochemistry, 62*(1), 169-191. https://doi.org/10.2138/rmg.2006.62.8

Berry, A. J., Hermann, J. r., O'Neill, H. S. C., & Foran, G. J. (2005). Fingerprinting the water site in mantle olivine. *Geology, 33*(11), 869-872. https://doi.org/10.1130/G21759.1

Bolfan-Casanova, N., Schiavi, F., Novella, D., Bureau, H., Raepsaet, C., Khodja, H., & Demouchy, S. (2018). Examination of Water Quantification and Incorporation in Transition Zone Minerals: Wadsleyite, Ringwoodite and Phase D Using ERDA (Elastic Recoil Detection Analysis). *Frontiers in Earth Science, 6*(75). Original Research. https://www.frontiersin.org/article/10.3389/feart.2018.00075

Daly, L., Lee, M. R., Bagot, P., Halpin, J., Smith, W., McFadzean, S., et al. (2020). Exploring Mars at the nanoscale: Applications of transmission electron microscopy and atom probe tomography in planetary exploration. *IOP Conference Series: Materials Science and Engineering, 891*, 012008. http://dx.doi.org/10.1088/1757-899X/891/1/012008

Demouchy, S. (2010a). Diffusion of hydrogen in olivine grain boundaries and implications for the survival of water-rich zones in the Earth's mantle. *Earth and Planetary Science*

Letters, *295*(1), 305-313. https://www.sciencedirect.com/science/article/pii/S0012821X10002578

Demouchy, S. (2010b). Hydrogen diffusion in spinel grain boundaries and consequences for chemical homogenization in hydrous peridotite. *Contributions to Mineralogy and Petrology*, *160*(6), 887-898. https://doi.org/10.1007/s00410-010-0512-4

Demouchy, S., & Bolfan-Casanova, N. (2016). Distribution and transport of hydrogen in the lithospheric mantle: A review. *Lithos*, *240-243*, 402-425. https://www.sciencedirect.com/science/article/pii/S002449371500417X

Devaraj, A., Colby, R., Hess, W. P., Perea, D. E., & Thevuthasan, S. (2013). Role of Photoexcitation and Field Ionization in the Measurement of Accurate Oxide Stoichiometry by Laser-Assisted Atom Probe Tomography. *The Journal of Physical Chemistry Letters*, *4*(6), 993-998. https://doi.org/10.1021/jz400015h

Drury, M. R. (1991). Hydration-Induced Climb Dissociation of Dislocations in Naturally Deformed Mantle Olivine. *Physics and Chemistry of Minerals*, *18*(2), 106-116. <Go to ISI>://WOS:A1991GA45600002

Dubosq, R., Gault, B., Hatzoglou, C., Schweinar, K., Vurpillot, F., Rogowitz, A., et al. (2020). Analysis of nanoscale fluid inclusions in geomaterials by atom probe tomography: Experiments and numerical simulations. *Ultramicroscopy*, *218*, 113092.

Gault, B., Moody, M. P., Cairney, J. M., & Ringer, S. P. (2012). *Atom Probe Microscopy* (Vol. 160). London: Springer.

Gault, B., Saxey, D. W., Ashton, M. W., Sinnott, S. B., Chiaramonti, A. N., Moody, M. P., & Schreiber, D. K. (2016). Behavior of molecules and molecular ions near a field emitter.

New Journal of Physics, *18*(3), 033031. http://dx.doi.org/10.1088/1367-2630/18/3/033031

Heggie, M. I. (1992). A molecular water pump in quartz dislocations. *Nature*, *355*(6358), 337-339. https://doi.org/10.1038/355337a0

Hiraga, T., Anderson, I. M., & Kohlstedt, D. L. (2004). Grain boundaries as reservoirs of incompatible elements in the Earth's mantle. *Nature*, *427*(6976), 699-703. https://doi.org/10.1038/nature02259

Johnson, L. J. S., Thuvander, M., Stiller, K., Oden, M., & Hultman, L. (2013). Blind deconvolution of time-of-flight mass spectra from atom probe tomography. *Ultramicroscopy*, *132*, 60-64. <Go to ISI>://WOS:000324235500011

Johnson, L. J. S., Thuvander, M., Stiller, K., Odén, M., & Hultman, L. (2013). Blind deconvolution of time-of-flight mass spectra from atom probe tomography. *Ultramicroscopy*, *132*, 60-64. https://www.sciencedirect.com/science/article/pii/S0304399113000855

Karato, S. (1990). The role of hydrogen in the electrical conductivity of the upper mantle. *Nature*, *347*(6290), 272-273. https://doi.org/10.1038/347272a0

Kaspar, T. C., Taylor, S. D., Yano, K. H., Lach, T. G., Zhou, Y., Zhu, Z., et al. (2021). Bulk and Short-Circuit Anion Diffusion in Epitaxial Fe2O3 Films Quantified Using Buried Isotopic Tracer Layers. *Advanced Materials Interfaces*, *8*(9), 2001768. https://onlinelibrary.wiley.com/doi/abs/10.1002/admi.202001768

Khisina, N., & Wirth, R. (2002). Hydrous olivine (Mg1-y Fe2+y)2-x vx SiO4H2x- a new DHMS phase of variable composition observed as nanometer-sized precipitations in mantle olivine. *Physics and Chemistry of Minerals*, *29*, 98-111.

Koga, K., Hauri, E., Hirschmann, M., & Bell, D. (2003). Hydrogen concentration analyses using SIMS and FTIR: Comparison and calibration for nominally anhydrous minerals. *Geochemistry Geophysics Geosystems*, *4*. <Go to ISI>://WOS:000181078500001

Krivolutskaya, N. A., & Bryanchaninova, N. I. (2011). Olivines of igneous rocks. *Russian Journal of General Chemistry*, *81*(6), 1302-1314. https://doi.org/10.1134/S1070363211060363

Kurosawa, M., Yurimoto, H., Matsumoto, K., & Sueno, S. (1992). Hydrogen analysis of mantle olivine by secondary ion mass spectrometry. *Washington DC American Geophysical Union Geophysical Monograph Series*, *67*, 283. https://ui.adsabs.harvard.edu/abs/1992GMS....67..283K

Lee, M. R., Tomkinson, T., Hallis, L. J., & Mark, D. F. (2015). Formation of iddingsite veins in the martian crust by centripetal replacement of olivine: Evidence from the nakhlite meteorite Lafayette. *Geochimica et Cosmochimica Acta*, *154*, 49-65. https://www.sciencedirect.com/science/article/pii/S0016703715000332

Meisenkothen, F., Samarov, D. V., Kalish, I., & Steel, E. B. (2020). Exploring the accuracy of isotopic analyses in atom probe mass spectrometry. *Ultramicroscopy*, *216*, 113018. https://www.sciencedirect.com/science/article/pii/S030439912030005X

Miller, & Forbes. (2014). *Atom-Probe Tomography: The Local Electrode Atom Probe*: Springer US.

Miller, M. K. (2000). *Atom Probe Tomography: Analysis at the Atomic Level*. New York: Kluwer Acedemic/Plenum Publishers.

Mosenfelder, J. L., Sharp, T., Asimow, P. D., & Rossman, G. R. (2006). Hydrogen Incorporation in Natural Mantle Olivines. *Earth's Deep Water Cycle, Geophys. Monogr. Ser., 108*, 45-56.

Peña, F. d. l., Prestat, E., Fauske, V. T., Burdet, P., Furnival, T., Jokubauskas, P., et al. (2021). hyperspy/hyperspy: Release v1.6.4. Retrieved from https://doi.org/10.5281/zenodo.5082777

Peslier, A. H. (2010). A review of water contents of nominally anhydrous natural minerals in the mantles of Earth, Mars and the Moon. *Journal of Volcanology and Geothermal Research, 197*(1), 239-258. https://www.sciencedirect.com/science/article/pii/S0377027309004028

Potrafke, A., Breiter, K., Ludwig, T., Neuser, R. D., & Stalder, R. (2020). Variations of OH defects and chemical impurities in natural quartz within igneous bodies. *Physics and Chemistry of Minerals, 47*(5), 24. https://doi.org/10.1007/s00269-020-01091-w

Qafoku, O., Kovarik, L., Kukkadapu, R. K., Ilton, E. S., Arey, B. W., Tucek, J., & Felmy, A. R. (2012). Fayalite dissolution and siderite formation in water-saturated supercritical CO2. *Chemical Geology, 332-333*, 124-135. https://www.sciencedirect.com/science/article/pii/S000925411200455X

Reddy, S. M., Saxey, D. W., Rickard, W. D. A., Fougerouse, D., Montalvo, S. D., Verberne, R., & van Riessen, A. (2020). Atom Probe Tomography: Development and Application to the Geosciences. *Geostandards and Geoanalytical Research, 44*(1), 5-50. https://doi.org/10.1111/ggr.12313. https://doi.org/10.1111/ggr.12313

Sommer, H., Regenauer-Lieb, K., Gasharova, B., & Siret, D. (2008). Grain boundaries: a possible water reservoir in the Earth's mantle? *Mineralogy and Petrology, 94*(1), 1-8. https://doi.org/10.1007/s00710-008-0002-9

Withers, A. C., Bureau, H., Raepsaet, C., & Hirschmann, M. M. (2012). Calibration of infrared spectroscopy by elastic recoil detection analysis of H in synthetic olivine. *Chemical Geology, 334*, 92-98.

https://www.sciencedirect.com/science/article/pii/S0009254112004901